

Repeating fast radio bursts from synchrotron maser radiation in localized plasma blobs: Application to FRB 20121102A

Xiao Li¹, Fen Lyu^{2,1}, Hai Ming Zhang¹, Can-Min Deng¹, and En-Wei Liang¹

¹ Guangxi Key Laboratory for Relativistic Astrophysics, School of Physical Science and Technology, Guangxi University, Nanning 530004, China

e-mail: lyufen@aqnu.edu.cn, lew@gxu.edu.cn

² Institute of Astronomy and Astrophysics, School of Mathematics and Physics, Anqing Normal University, Anqing 246133, People's Republic of China

Received XXX / Accepted XXX

ABSTRACT

The radiation physics of repeating fast radio bursts (FRBs) remains enigmatic. Motivated by the observed narrow-banded emission spectrum and ambiguous fringe pattern of the spectral peak frequency (ν_{pk}) distribution of some repeating FRBs, such as FRB 20121102A, we propose that the bursts from repeating FRBs arise from synchrotron maser radiation in localized blobs within weakly magnetized plasma that relativistically moves toward observers. Assuming the plasma moves toward the observers with a bulk Lorentz factor of $\Gamma = 100$ and the electron distribution in an individual blob is monoenergetic ($\gamma_e \sim 300$), our analysis shows that bright and narrow-banded radio bursts with peak flux density ~ 1 Jy at peak frequency ($\nu_{\text{pk}} \sim 3.85$ GHz) can be produced by the synchrotron maser emission if the plasma blob has a magnetization factor of $\sigma \sim 10^{-5}$ and a frequency of $\nu_p \sim 4.5$ MHz. The spectrum of bursts with lower ν_{pk} tends to be narrower. Applying our model to the bursts of FRB 20121102A, the distributions of both the observed ν_{pk} and isotropic energy E_{iso} detected by the Arecibo telescope at the L band and the Green Bank Telescope at the C band are successfully reproduced. We find that the ν_p distribution exhibits several peaks, similar to those observed in the ν_{pk} distribution of FRB 20121102A. This implies that the synchrotron maser emission in FRB 20121102A is triggered in different plasma blobs with varying ν_p , likely due to the inhomogeneity of relativistic electron number density.

Key words. Radio transient sources; masers-plasma; Radio bursts; Individual FRB 20121102A

1. Introduction

Fast radio bursts (FRBs) are bright radio transients that last several to tens of milliseconds and are mostly extragalactic, with a typical dispersion measure (DM) of $\sim 100 - 3038$ pc cm⁻³ (Lorimer et al. 2007; Keane et al. 2012; Thornton et al. 2013; Cordes & Chatterjee 2019; Petroff et al. 2019, 2022; Bhardwaj et al. 2021; CHIME/FRB Collaboration et al. 2021). More than 800 FRBs have been detected to date (Petroff et al. 2016; CHIME/FRB Collaboration et al. 2021), over 60 of which exhibit repetitive behaviors (Fonseca et al. 2020; Chime/Frb Collaboration et al. 2023)¹. Similar to the spectra of one-off FRBs, the spectra of bursts from individual repeating FRB sources display significant diversity (Spitler et al. 2016; Macquart et al. 2019). However, repeating FRBs typically exhibit longer durations and narrower bandwidths than one-off FRBs (CHIME/FRB Collaboration et al. 2021; Pleunis et al. 2021). Bursts from repeating FRB sources often exhibit complex time-frequency drift structures, and some bursts consist of several sub-bursts (Hessels et al. 2019; Zhou et al. 2022). The question of whether all FRBs are repeating remains unresolved (Caleb et al. 2019; Zhong et al. 2022).

The origin of FRBs is still unclear and widely debated (see Platts et al. 2019; Zhang 2023 for reviews). Most proposed source models involve some compact objects, such as magnetized neutron stars (Dai et al. 2016; Wang et al. 2016), young pulsars (Lyutikov et al. 2016; Lyu et al. 2021), magnetars

(Lyubarsky 2014; Beloborodov 2017, 2020; Metzger et al. 2019; Lu et al. 2020), strange stars (Zhang et al. 2018a; Geng et al. 2021), and black holes (Katz 2020; Deng 2021). The detected association of magnetar SGR 1935+2154 with FRB 20200428 suggests that at least some FRBs may originate from magnetars (Bochenek et al. 2020; CHIME/FRB Collaboration et al. 2020).

The observed spectral profiles of bursts from repeating FRBs are typically modeled with a Gaussian function (Law et al. 2017; Aggarwal et al. 2021; Zhou et al. 2022). These bursts are generally narrow-banded. For instance, the spectra of bursts emitted by FRB 20201124A have a characteristic bandwidth ($\Delta\nu$) of ~ 0.277 GHz, with a peak frequency (ν_{pk}) of 1.09 GHz (Zhou et al. 2022). The relative spectral bandwidth $\Delta\nu/\nu_{\text{pk}}$ for 1076 bursts from FRB 20220912A, detected by the Five-hundred-meter Aperture Spherical Radio Telescope (FAST, Jiang et al. 2019), is narrowly distributed in the range (0.1 \sim 0.2) (Zhang et al. 2023). For one burst from repeating FRB 20190711A, $\Delta\nu/\nu_{\text{pk}}$ is 0.065/1.4 (Kumar et al. 2021). These observations suggest that the narrow spectra of these typical FRBs are likely intrinsic and determined by their intrinsic radiation mechanism (Yang 2023; Wang et al. 2024).

Multiple frequency observations, particularly wideband frequency observations, are critical for understanding the radiation mechanism of FRBs. FRB 20121102A, the first detected repeating FRB source (Spitler et al. 2016), has had thousands of bursts reported by various monitoring campaigns across 0.5 – 8 GHz (e.g., Spitler et al. 2014; Gajjar et al. 2018; Zhang et al. 2018b; Houben et al. 2019; Josephy et al. 2019; Oostrum et al. 2020; Ra-

¹ <https://blinkverse.zero2x.org/>

jwade et al. 2020; Li et al. 2021; Hewitt et al. 2022). It has a typical $\Delta\nu$ less than 500 MHz (Gajjar et al. 2018; Lyu et al. 2022). Moreover, the peak frequency of bursts observed by the Green Bank Telescope (GBT) at the C band (4 – 8 GHz) shows several discrete peaks (Gajjar et al. 2018; Zhang et al. 2018b; Lyu et al. 2022). Interestingly, when extending such a fringe spectral feature to 0.5 – 4 GHz, the bimodal burst energy distribution observed with FAST by Li et al. (2021) can be well reproduced by assuming a simple power law energy function (Lyu et al. 2022). Similar discrete peaks are also seen in the peak frequency distributions of repeating FRB sources FRB 20190520B and FRB 20201124A (Lyu & Liang 2023; Lyu et al. 2024).

The high brightness temperature ($T_B \geq 10^{35}$ K) indicates that the radiation mechanism of FRBs must be coherent (Zhang 2020; Lyubarsky 2021; Xiao et al. 2021). Various hypotheses have been proposed, such as synchrotron maser radiation in relativistic shocks under strong magnetization conditions (Lyubarsky 2014; Beloborodov 2017, 2020; Metzger et al. 2019) or weak magnetization conditions (Waxman 2017) as well as vacuum conditions (Ghisellini 2017), coherent curvature radiation, coherent inverse Compton scattering, or coherent Cherenkov radiation close in the magnetosphere (Yang & Zhang 2018; Zhang 2022; Liu et al. 2023). Synchrotron maser radiation under weak magnetization conditions has a very narrow intrinsic radiation spectrum and a prominent peak (Sagiv & Waxman 2002). Inspired by the observed narrow-banded emission spectrum and the fringe pattern of the ν_{pk} distribution of repeating FRBs, we explore whether the synchrotron maser radiation mechanism of electrons in a weakly magnetized relativistic plasma can account for these spectral characteristics.

The paper is organized as follows. The model is presented in Sect. 2. The application of our model to explain the spectral characteristics of FRB 20121102A and to constrain the model parameters via Monte Carlo simulations is shown in Sect. 3. Conclusions and discussion are given in Sect. 4. Throughout the paper, we adopt a flat Λ CDM cosmology with cosmological parameters $H_0=67.7$ km s⁻¹ Mpc⁻¹, $\Omega_m = 0.31$ (Planck Collaboration et al. 2016).

2. Model

We propose that repeating FRBs arise from a pre-accelerated plasma that relativistically moves toward observers with a bulk Lorentz factor of Γ . It may originate from a relativistic outflow powered by the central engine (e.g., Lyubarsky 2014; Waxman 2017; Metzger et al. 2019; Beloborodov 2020; Khangulyan et al. 2022). A burst episode results from plasma instability induced by ejecta injected from the activity of the central engine, such as magnetar flares. The ejecta is highly relativistic and may be dominated by Poynting flux or baryons. The interaction between the ejecta and the plasma shell generates collisionless shocks, which induce plasma instability or turbulence and form localized blobs. In case of the synchrotron maser emission conditions are satisfied in some blobs, bright FRB events with a narrow-banded spectrum can be generated by the synchrotron maser radiation of electrons in the plasma blobs (e.g., Sagiv & Waxman 2002; Waxman 2017; Gruzinov & Waxman 2019). The observed frequency-dependent depolarization may be due to the FRB emission propagation through the clumpy shell (Xu et al. 2022; Feng et al. 2022).

We show the cartoon of our model in Fig. 1. The size of the blob in the comoving frame is estimated as $R' = \Gamma c \Delta t \sim 3 \times 10^9$ cm, assuming $\Gamma = 100$ and $\Delta t = 1$ ms. The plasma frequency is given by $\nu_p = (n_e e^2 / \pi \gamma_e m_e)^{1/2}$ and the magnetization factor is

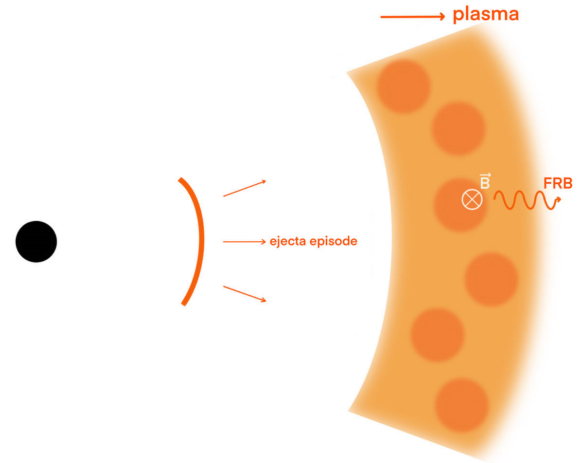


Fig. 1. Schematic configuration: the ejecta from the central engine triggers plasma instabilities, inducing localized electron plasma blobs that generate FRBs.

defined as $\sigma = B^2 / 4\pi m_e c^2 \gamma_e n_e = (\nu_B / \nu_p)^2$, where n_e is the relativistic number density of electrons, e is the electron charge, m_e is the rest mass of the electron, B is the magnetic field, γ_e is the Lorentz factor of the electron and ν_B is the cyclotron frequency of the relativistic electron (Lyubarsky 2021).

The synchrotron radiation power of a relativistic electron in the plasma is severely suppressed for emission at $\nu \lesssim \nu_{R^*}$. This suppression is known as the Razin effect². Another striking effect of synchrotron radiation in the plasma is the maser emission mechanism, which involves the amplification of radiation caused by the negative synchrotron self-absorption (Twiss 1958; McCray 1966; Zheleznyakov 1967; Sazonov 1970; Sagiv & Waxman 2002; Waxman 2017). The self-absorption coefficient for a specific polarization mode of synchrotron radiation is given by (Ginzburg 1989; Sagiv & Waxman 2002)

$$\alpha_v^{[\perp, \parallel]} = -\frac{1}{4\pi m_e v^2} \int d\gamma_e \gamma_e^2 P_v^{[\perp, \parallel]}(\gamma_e) \frac{d}{d\gamma_e} \left(\gamma_e^{-2} \frac{dn_e}{d\gamma_e} \right) \quad (1)$$

and

$$P_v^{[\perp, \parallel]}(\gamma_e) = \frac{\sqrt{3} e^3 B \sin \chi}{2m_e c^2} \left[1 + \left(\frac{\nu_R}{\nu} \right)^2 \right]^{-1/2} \frac{\nu}{\tilde{\nu}_c} \times \left[\int_{\nu/\tilde{\nu}_c}^{\infty} K_{5/3}(z) dz \pm K_{2/3} \left(\frac{\nu}{\tilde{\nu}_c} \right) \right], \quad (2)$$

where $P_v^{[\perp, \parallel]}(\gamma_e)$ is the radiation power per unit frequency emitted by a single electron with Lorentz factor γ_e in a polarization

² The synchrotron emission beaming angle of a relativistic electron in the plasma is given by $\theta = \sqrt{1 - n^2 \beta^2}$, where n represents the refractive index ($n^2 \approx 1 - \nu_p^2 / \nu^2 \neq 1$) and β is the velocity of the electron in units of speed of the light (Rybicki & Lightman 1986). In the case of $\nu \approx 1$, we have $\theta \approx \sqrt{1 - n^2} = \nu_p / \nu$, indicating that the beaming angle depends on both the emission frequency and plasma frequency. For a certain emission frequency below ν_R (the so-called Razin frequency $\gamma_e \nu_p$), its beaming angle is significantly larger than that in the vacuum, $\nu_p / \nu \gg 1 / \gamma_e$, resulting in a significant weakening of the beaming effect (McCray 1966; Rybicki & Lightman 1986). Furthermore, Sagiv & Waxman (2002) generalized the typical frequency at which the beaming effect is weakened to $\nu \lesssim \nu_{R^*} = \nu_p \min \{ \sigma^{-1/4}, \gamma_e \}$, where ν_{R^*} is the modified Razin frequency.

mode $[\perp, \parallel]$. Here, \perp and \parallel denote the linear polarization perpendicular and parallel to the projection of the magnetic field on the plane of observation, respectively. χ is the pitch angle, $K_{5/3}$ and $K_{2/3}$ are the modified Bessel functions, and

$$\tilde{\nu}_c = \frac{3eB \sin \chi}{4\pi m_e c} \gamma_e^2 \left[1 + \left(\frac{\nu_R}{\nu} \right)^2 \right]^{-3/2}. \quad (3)$$

The contribution of the negative reabsorption comes from the regions where the electron distribution function is steeper than γ_e^2 (Sagiv & Waxman 2002; Waxman 2017; Gruzinov & Waxman 2019). McCray (1966) and Zheleznyakov (1967) discussed the possibility of negative reabsorption in cold plasma (non-relativistic plasma). However, even without cold plasma, due to the correction of n by relativistic electron plasma, negative reabsorption can occur at $\nu \lesssim \nu_R$ when $\gamma_e^2 \ll \sigma^{-1/2}$ (Sazonov 1970). Sagiv & Waxman (2002) derived that negative reabsorption can also occur below the frequency $\sigma^{-1/4} \nu_p$ even when $\gamma_e^2 > \sigma^{-1/2} > 1$. Finally, it is generally believed that negative reabsorption occurs at $\nu \lesssim \nu_{R^*} = \nu_p \min \{ \sigma^{-1/4}, \gamma_e \}$. Following Sagiv & Waxman (2002); Waxman (2017), negative reabsorption can arise from a narrow electron distribution. In our analysis, we assume that the electron distribution in the blobs is monoenergetic as $\frac{dn_e}{d\gamma_e} = n_e \delta(\gamma_e - \gamma_{e,s})$. Moreover, FRB 20121102A shows almost 100% linear polarization degree (Michilli et al. 2018). Therefore, the reabsorption coefficient of the radiation produced by a monoenergetic electron distribution is given as

$$\alpha_v^{[\perp]} = \alpha_0 F^{[\perp]} \left[\gamma_{e,s}^2 \sigma^{1/2}, \frac{\nu}{\nu_{R^*}} \right], \quad \alpha_0 = \frac{\pi \nu_p}{2 \sqrt{3} c} \sigma^{-3/4} \sin \chi. \quad (4)$$

The details of the function $F^{[\perp]}$ are given in Eq. (A.5) in the Appendix. We present the numerical results of our model by considering $\gamma_{e,s}^2 \sigma^{1/2}$ values of 2, 5, 10, 20, 50, 100, and 1000, with $\chi = \pi/4$. Figure 2 shows the normalized self-absorption coefficient ($\alpha_v^{[\perp]}/\alpha_0$) as a function of the frequency in units of ν_{R^*} in the comoving frame. It is observed that negative reabsorption begins at $\nu/\nu_{R^*} \sim 0.4$, independent of the $\gamma_{e,s}^2 \sigma^{1/2}$ values. The peak negative reabsorption and the corresponding frequency are parameter dependent at $\gamma_{e,s}^2 \sigma^{1/2} < 50$, but they approach an asymptotic value of ($\alpha_v^{[\perp]}/\alpha_0$) = -0.4 at $\nu = 0.70 \nu_{R^*}$ by increasing the values of $\gamma_{e,s}^2 \sigma^{1/2}$ up to 1000. The negative reabsorption regime is confined in the frequency range of $0.4 \nu_{R^*} < \nu < \nu_{R^*}$. The gray solid line in Fig. 2 represents the positive self-absorption coefficient against frequency neglecting the plasma effects (The detailed calculation is shown in Eq. (A.8) in Appendix).

The radiation intensity is given by (e.g., Sagiv & Waxman 2002)

$$I_\nu = j_\nu \Delta \frac{1 - e^{-\tau_\nu}}{\tau_\nu}, \quad (5)$$

where j_ν is the specific emissivity (see Appendix Eq. (A.3) for details), τ_ν is the optical depth and Δ is the width of the radiating region along the line of sight. The specific emissivity of a single electron plasma blob is given as

$$j_\nu^{[\perp]} = j_0 G^{[\perp]} \left[\gamma_{e,s}^2 \sigma^{1/2}, \frac{\nu}{\nu_{R^*}} \right], \quad j_0 = \frac{\pi m_e}{2 \sqrt{3} c} \nu_p^3 \sin \chi. \quad (6)$$

The details of the function $G^{[\perp]}$ are given in Eq. (A.6) in the Appendix. Therefore, the radiation flux density of an individual blob in the observer's frame can be estimated as (Zhang 2018)

$$F_\nu(\nu_{\text{obs}}) = \frac{(1+z)\Gamma^3 j_\nu^{[\perp]}(\nu') \frac{1 - e^{-\tau_\nu^{[\perp]}(\nu')}}{\tau_\nu^{[\perp]}(\nu')} V'}{D_L^2}, \quad (7)$$

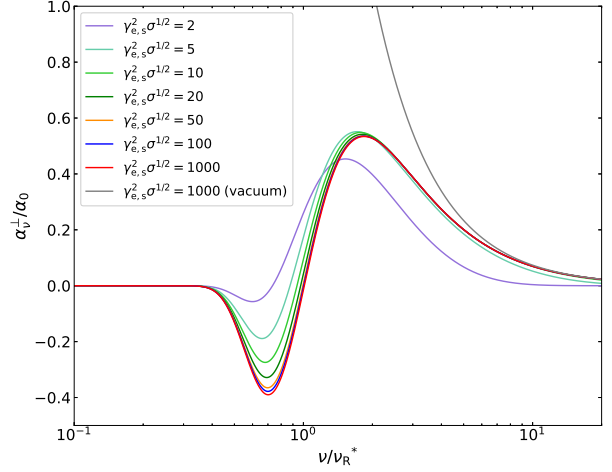


Fig. 2. Normalized self-absorption coefficient for \perp polarization, given a single-energy electron distribution and $\chi = \frac{\pi}{4}$, is plotted against frequency normalized by the scaling factor ν_{R^*} . The gray solid line represents the results obtained without plasma effects.

where the prime means that the corresponding quantities are measured in the comoving frame, z is the redshift, V' is the volume, and D_L is the luminosity distance. The peak frequency of emission in the observer's frame can be estimated as

$$\nu_{\text{pk}} = (1+z)^{-1} 0.70 \sigma^{-1/4} \nu_p \Gamma = 0.70 (1+z)^{-1} \Gamma_2 \sigma_{-4}^{-1/4} \nu_{p,6} \text{ GHz}, \quad (8)$$

where notation $Q_n = Q/10^n$ is adopted in the cgs units. In our model, the volume and optical depth of a single blob are denoted as $4\pi R^3/3$ and $\alpha_v^{[\perp]} R'$, respectively. Taking $\gamma_{e,s} = 300$, $\sigma = 2.2 \times 10^{-5}$, $\Gamma = 100$, $\nu_p = 4.5$ MHz, $D_L = 1$ Gpc ($z = 0.193$), and $t = 1$ ms, we derive the radiating spectrum as shown in the top panel of Fig. 3. Its peak frequency is $\nu_{\text{pk}} = 3.85$ GHz and its peak flux density is $F_{\nu_{\text{pk}}} = 1.13$ Jy. One can observe that the synchrotron maser emission can generate extremely narrow spectra and exceptionally bright signals (with peak flux density exceeding the emission in other bands by more than 12 orders of magnitude) at GHz frequency. For illustrating the spectral shapes in the energy bands of the GBT and Arecibo telescopes, Fig. 3 (bottom) also shows the predicted spectra above the detection thresholds of the GBT ($F_{\text{limit}} = 0.0265$ Jy) and the Arecibo telescope ($F_{\text{limit}} = 0.057$ Jy) by employing three parameter sets as marked in the panel with fixing $\Gamma = 100$. It can be observed that our model predicts the narrower spectrum with the lower peak frequency.

3. Application to FRB 20121102A

The rich observational data across multiple frequencies of FRB 20121102A makes it a good candidate for exploring the radiation mechanism of FRBs. Its high brightness temperature ($T_B \geq 10^{35}$ K) indicates that its radiation mechanism must be coherent. Its redshift is $z = 0.193$ ($D_L = 972$ Mpc) (Tendulkar et al. 2017) and the typical burst duration is $t_{\text{obs}} = 1$ ms. The distribution of burst energy ranges from 4×10^{36} to 10^{40} erg (Li et al. 2021). The observed spectral profile follows a Gaussian function (Law et al. 2017; Aggarwal et al. 2021). Interestingly, the distribution of peak frequency of FRB 20121102A observed with

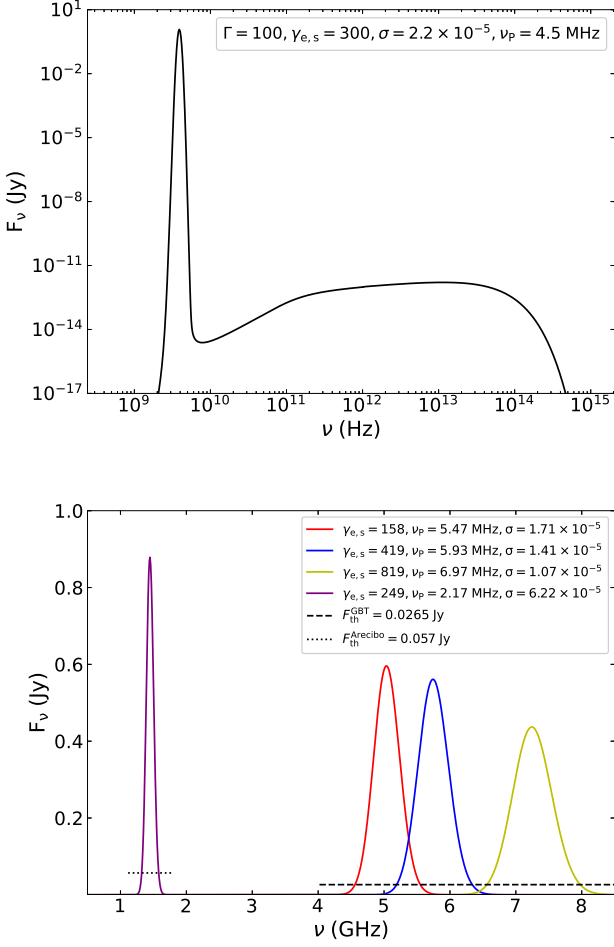


Fig. 3. Flux density of synchrotron radiation as a function of frequency for FRBs, assuming a monoenergetic electron population in an individual blob (top panel). The predicted “observable” burst spectral profiles under different parameters range from 1 to 8 GHz (bottom panel).

GBT at the C band exhibits a putative fringe pattern, and such a feature also seems to be seen in the observation with the Arecibo telescope at the L band (1.15 – 1.73 GHz) (Lyu et al. 2022). We analyze these spectral properties with our model through Monte Carlo simulations.

Our simulation analysis is based on the observations of the peak frequency $\nu_{\text{pk}}^{\text{obs}}$ and the isotropic energy $E_{\text{iso}}^{\text{obs}}$ from the GBT and Arecibo telescopes. Assuming the emitting region is a pre-accelerated plasma that moves toward observers with a bulk Lorentz factor $\Gamma = 100$, we explore the model parameter set $\{\gamma_{e,s}, \sigma, \nu_p\}$ that can represent the $\nu_{\text{pk}}^{\text{obs}}$ and $E_{\text{iso}}^{\text{obs}}$ distributions observed with the GBT and Arecibo telescopes. Below, we outline our simulation procedure for the GBT observation.

1. We generate a $\nu_{\text{pk}}^{\text{sim}}$ value from the $\nu_{\text{pk}}^{\text{obs}}$ distribution observed by the GBT (Gajjar et al. 2018; Zhang et al. 2018b). Lyu et al. (2022) fitted the $\nu_{\text{pk}}^{\text{obs}}$ distribution with a multi-Gaussian function. We adopt the fitting results from Lyu et al. (2022) and generate $\nu_{\text{pk}}^{\text{sim}}$ based on the derived probability distribution.
2. We generate a set of $\{\gamma_{e,s}, \sigma\}$ assuming that they are uniformly distributed in the range of $\gamma_{e,s} \in [2, 10^3]$ and $\sigma \in [\gamma_{e,s}^{-4}, 1)$, where the distribution range of σ is derived from

the weak magnetization condition ($\gamma_{e,s}^2 > \sigma^{-1/2} > 1$). When $\gamma_{e,s}^2 \sigma^{-1/2} > 50$, we calculate the ν_p value with Eq. (8). We calculate the simulated peak flux density ($F_{\nu_{\text{pk}}}^{\text{sim}}$) at $\nu_{\text{pk}}^{\text{sim}}$ with Eq. (7) for the parameter set of $\{\gamma_{e,s}, \sigma, \nu_p\}$. We check whether the $F_{\nu_{\text{pk}}}^{\text{sim}}$ value is in the range of $0.015 \text{ Jy} < F_{\nu_{\text{pk}}}^{\text{sim}} < 0.8 \text{ Jy}$ as observed with GBT. If it does, we choose the parameter set and proceed to the next step. Otherwise, we discard this parameter set and repeat this step.

3. We calculate the burst isotropic energy with

$$E_{\text{iso}}^{\text{sim}} = \left(10^{36} \text{ erg}\right) \frac{4\pi}{1+z} \left(\frac{D_L}{10^{28} \text{ cm}}\right)^2 \frac{F_{\nu_{\text{pk}}}^{\text{sim}}}{\text{Jy}} \frac{\nu_{\text{pk}}^{\text{sim}}}{\text{GHz}} \frac{\Delta t}{\text{ms}},$$

where Δt is the burst duration. Our analysis takes the typical value with $\Delta t = 1 \text{ ms}$.

4. We repeat the above steps to generate a sample of 5×10^4 bursts, then extract a sub-sample of 8×10^3 bursts by utilizing the accumulated probability distribution function $[\psi(E_{\text{iso}}^{\text{obs}})]$ for $E_{\text{iso}}^{\text{obs}}$. To do so, we generate 8×10^3 random numbers in the range of (0,1) and set them as the values of ψ , then identify the corresponding $E_{\text{iso}}^{\text{sim}}$ values with the inverse function of $\psi(E_{\text{iso}}^{\text{obs}})$.

Each simulated burst is characterized by $\{\nu_{\text{pk}}^{\text{sim}}, E_{\text{iso}}^{\text{sim}} | \gamma_{e,s}, \sigma, \nu_p\}$. The parameters of the plasma, namely $\gamma_{e,s}$, σ , and ν_p , are constrained by the consistency of the ν_{pk} and E_{iso} distributions between the observed and simulated samples. Similarly, we also simulate the Arecibo telescope observations (Hewitt et al. 2022) with the same approach. We select only those bursts whose high (ν_{high}) and low (ν_{low}) frequencies are available because the main emission of these bursts is detected within the bandwidth of the Arecibo telescope. Since the peak flux density of these bursts is not presented in Hewitt et al. (2022), we use the observed fluence in a 1 ms peak time as a proxy for the peak flux density. Figure 4 compares the distributions of ν_{pk} and E_{iso} between the observed and simulated samples. We measure their consistency with the Kolmogorov-Smirnov test. The derived p-values are larger than 0.1, indicating that the distributions of ν_{pk} and E_{iso} between the simulated and observed samples are statistically consistent.

Figure 5 illustrates the histograms of the model parameters derived from our analysis. For the bursts in the 4 – 8 GHz band, the $\gamma_{e,s}$ is uniformly distributed in the range of $110 < \gamma_{e,s} < 3000$, and the distribution of σ ranges from 9×10^{-6} to 2×10^{-5} . For the bursts in the 1.15 – 1.73 GHz band, the $\gamma_{e,s}$ is uniformly distributed in the range of $80 < \gamma_{e,s} < 3000$, and the distribution of σ ranges from 4.7×10^{-5} to 7.4×10^{-5} . The distribution of ν_p shows several peaks in the range from $\log \nu_p / (\text{MHz}) = 6.70$ ($\nu_p = 5.00 \text{ MHz}$) to $\log \nu_p / (\text{MHz}) = 6.87$ ($\nu_p = 7.5 \text{ MHz}$) for the bursts observed with the GBT, and a narrow peak around $\log \nu_p / (\text{MHz}) = 6.35$ (2.2 MHz) for the bursts observed with the Arecibo telescope. The $\log \nu_p$ distribution is similar to the $\nu_{\text{pk}}^{\text{obs}}$ distribution, suggesting that the $\nu_{\text{pk}}^{\text{obs}}$ of a burst is sensitive to ν_p , hence to the relativistic electron number density in the radiating region.

4. Conclusions and discussion

This paper proposes that repeating FRBs arise from synchrotron maser radiation produced by a series of local electron plasma blobs in a weakly magnetized relativistic plasma, which are induced by plasma instabilities triggered by the injected ejecta

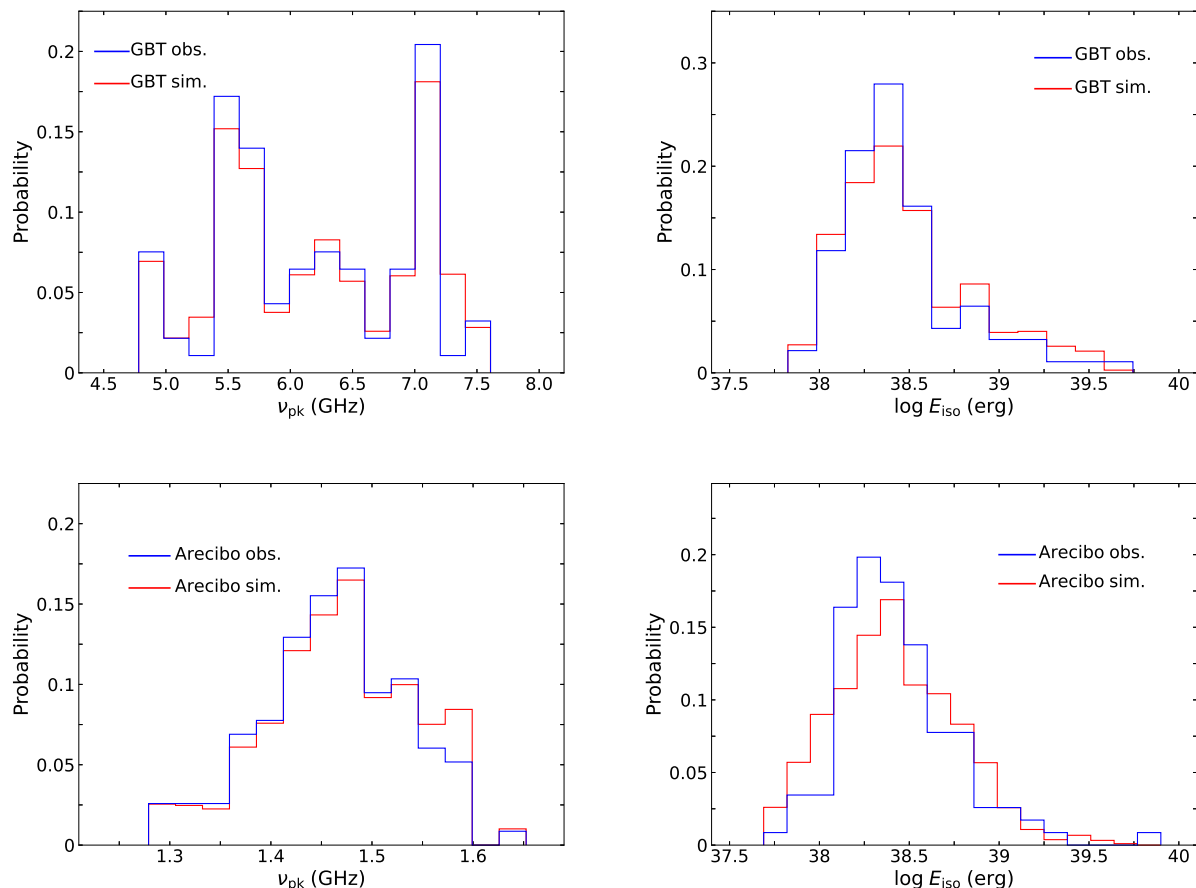


Fig. 4. Comparison of the peak frequency ν_{pk} and isotropic energy E_{iso} distributions between the simulated and observed samples, where the data of the observed samples are taken from [Lyu et al. \(2022\)](#).

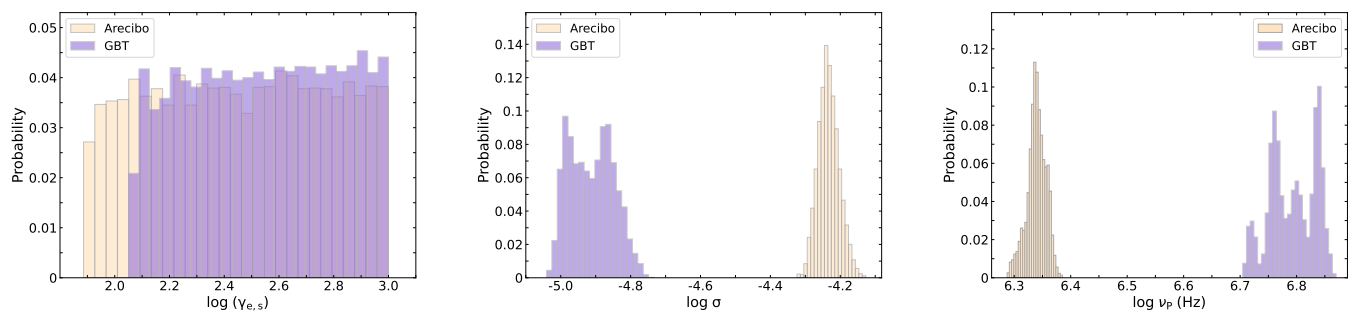


Fig. 5. Histograms of the model parameters $\gamma_{e,s}$, σ and ν_p derived from our simulation analysis.

from the central engine. We present the numerical calculation of the synchrotron maser radiation spectrum in FRBs, assuming a monoenergetic electron population within an individual blob. The negative reabsorption is toward a maximum at frequency $\nu_{\text{max}} = 0.70\Gamma\sigma^{-1/4}\nu_p$ if $\gamma_{e,s}^2\sigma^{1/2} > 50$. The peak flux density of synchrotron maser emission is $F_{\nu_{\text{pk}}} \sim \text{Jy}$ and the corresponding ν_{pk} is at several GHz, if $\sigma \sim 10^{-5}$, $\gamma_{e,s} > 100$, $\nu_p > 2$ MHz, and $\Gamma = 100$. Our model predicts that FRBs with lower peak frequencies have narrower intrinsic radiation spectra. We utilize our model to account for the observed ν_{pk} and E_{iso} characteristics of FRB 20121102A observed with the GBT and the Arecibo telescopes. Our analysis reveals that the ν_p distribution exhibits several peaks, which is similar to the $\nu_{\text{pk}}^{\text{obs}}$ distributions. This im-

plies that the $\nu_{\text{pk}}^{\text{obs}}$ of a burst is sensitive to ν_p , which represents the relativistic electron number density.

The synchrotron maser radiations result from the negative synchrotron self-absorption if the refractive index of the relativistic plasma is less than unity. It should be noted that the refractive index in a relativistic plasma depends on the energy and angular distribution of particles ([Aleksandrov et al. 1984](#)). In a weakly magnetized relativistic plasma environment, the refractive index of $n^2 = 1 - (\frac{\nu_p}{\nu})^2$ is valid for monoenergetic distribution and power law distribution of the electrons ([Sagiv & Waxman 2002](#)). Additionally, we can use the numerical results of the reabsorption coefficient to test the self-consistency of our calculations. As shown in [Ginzburg \(1989\)](#) and [Sagiv &](#)

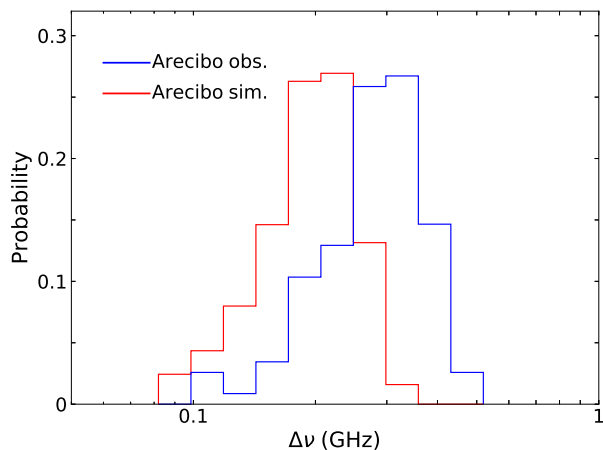


Fig. 6. Comparison of the spectral width $\Delta\nu$ of the observed sample detected by Arecibo telescope in [Hewitt et al. \(2022\)](#) with the simulated ones.

[Waxman \(2002\)](#), synchrotron maser emission is linearly polarized, if the conditions of $|1 - n| \gg |c\alpha_v/\nu|$ and $|\Delta n| \ll |\alpha_v c/\nu|$ are satisfied, where $|\Delta n|$ represents the difference in the refractive index between the circularly polarized modes introduced by the magnetic field. The synchrotron maser emission sharply peaks at $\nu \sim 0.70\nu_R^*$. Thus, we have $|1 - n| \sim \frac{\nu_p^2}{2\nu^2} = 1.02\sigma^{1/2}$, $\Delta n \sim \nu_p^2\nu_B/\nu^3 = 2.91\sigma^{5/4}$, and $\alpha_v c/\nu = 0.37\sigma$. Our analysis yields $\sigma \sim 10^{-5}$, indicating that these conditions are met. Thus, the maser emission is linearly polarized consistent with the observation of FRB 20121102A ([Michilli et al. 2018](#)).

The $\Delta\nu$ in the sample observed with the Arecibo telescope is available. We also calculate the simulated $\Delta\nu$ for the Arecibo sample and compare its distribution with the observed ones in [Fig. 6](#). It was found that they have similar distribution profiles, but the simulated $\Delta\nu$ distribution peaks at 0.2 GHz, while the observed peaks at 0.3 GHz. This discrepancy is possibly due to the propagation process broadening the spectra.

FRB 20121102A is located in a star-forming region of a dwarf galaxy ([Tendulkar et al. 2017](#)), and in an extremely dynamic magnetized ionized environment (high Faraday rotation measure $RM \sim 10^5$ rad m^{-2} , [Michilli et al. 2018](#)). It is spatially associated with a compact, persistent radio source (PRS) ([Chatterjee et al. 2017](#)). It also has a possible periodicity of approximately 160 days ([Rajwade et al. 2020](#); [Cruces et al. 2021](#)). Our analysis suggests that the synchrotron maser emission for FRB 20121102A is stimulated in a weakly magnetized region ($\sigma \sim 10^{-5}$). A small σ is primarily caused by a high relativistic electron number density. We approximate the electron population for generating the synchrotron maser emission as single-energy electrons and the derived relativistic electron density of $n_e = 10^6 \sim 10^8$ cm^{-3} . The hot corona region around accretion disk near compact objects (e.g., [Gruzinov & Waxman 2019](#)), in a binary system where compact stars undergo an accretion-induced explosion or episodic jets caused by accretion (e.g., [Long & Pe'er 2018](#); [Deng et al. 2021](#)), or in flare of weakly magnetized material generated by magnetars ([Khargulyan et al. 2022](#)), can offer such an environment.

The distribution of ν_{pk} observed in FRB 20121102A displays a fringe pattern³. Our model explains the observed fringe pattern with the inhomogeneity of relativistic electron density in plasma blobs. We note that [Feng et al. \(2022\)](#) suggested that the significant frequency-dependent depolarization at frequencies lower than 3.5 GHz in FRB 20121102A is caused by multipath propagation of the FRB emission through an inhomogeneous magnetic-ionic environment. The ν_{pk} distribution of FRB 20201102A is similar to the zebra radio spectrum typically seen in individual radio bursts emitted by the Sun and Crab ([Hankins & Eilek 2007](#); [Karlický 2013](#)). The zebra radio spectra of the solar or Crab radiations may also arise from a plasma radiation mechanism driven by uneven plasma density. [Karlický \(2013\)](#) proposed that the plasma density accumulation in different regions could be modulated by the magnetohydrodynamic waves in the radiation region. In addition, some energy release processes may form traps that can confine the plasma, similar to the magnetic trap proposed by [Kong et al. \(2019\)](#). Furthermore, if low-density cavities exist within the plasma, they could impose a discrete frequency structure on the radiation ([Hankins et al. 2016](#)).

The extensively discussed radiation models of FRBs can generally be divided into two categories: the “close-in” scenario, where the emission originates from coherent curvature radiation in the magnetosphere of magnetars (e.g., [Kumar et al. 2017](#); [Yang & Zhang 2018](#); [Lu et al. 2020](#)), and the “far-away” scenario, where the emission originates from synchrotron maser radiation in a relativistic outflow (e.g., [Lyubarsky 2014](#); [Waxman 2017](#); [Metzger et al. 2019](#); [Beloborodov 2020](#); [Khargulyan et al. 2022](#)). Our model is similar to the far-away scenario. Our model suggests that the inhomogeneity of the local relativistic plasma blobs is stimulated by the injection from the central engine. In our model, the ejecta is required to be highly relativistic, and it is likely similar to the magnetar flares from an active magnetar ([Lyubarsky 2014](#); [Metzger et al. 2019](#); [Khargulyan et al. 2022](#)).

Some repeating FRB sources show complex polarization behaviors, including frequency-dependent depolarization, variation of RM, and oscillating spectral structures of polarized components ([Feng et al. 2022](#)). As reported by [Feng et al. \(2022\)](#), the observed frequency-dependent depolarization and correlation between RM scatter and the temporal scattering time can be explained by multiple-path propagation through a complex environment, such as a supernova remnant-like, inhomogeneous, magnetized plasma screen (nebula) close to a repeating FRB source ([Yang et al. 2022](#)). This suggests that the temporal scattering and RM scatter originate from the same site. The model proposed by [Yang et al. \(2022\)](#) attributes the observed polarization variation to the propagation of the FRB emission in the nebula. They also suggested that the nebula can be responsible for the associated PRS emission. Differently, we argue that the outbursts and propagation of FRB bursts are in the same site, which is an inhomogeneous, weakly-magnetized plasma shell.

The repeating behavior of FRBs is attributed to the episodic activity of the central engine in the framework of our model (e.g., [Metzger et al. 2019](#)). Observations show that the duration of an outburst episode lasts from days to several months and the burst rates are erratic. For example, FRB 20201124A is a very active

³ Notably, the spectral fringe feature, observed within the range of 4 – 8 GHz, was derived from a statistical analysis of 93 bursts observed in 6 hours. Despite extensive multiwavelength monitoring campaigns have been conducted on FRB 20121102A using various telescopes (e.g., [Scholz et al. 2016](#); [Law et al. 2017](#); [Gourdji et al. 2019](#); [Houben et al. 2019](#); [Pearlman et al. 2020](#)), only one burst was simultaneously detected by Arecibo at 1.4 GHz and VLA at 3 GHz ([Law et al. 2017](#)).

FRB. The follow-up observation with the FAST telescope detected a significant activity, with the detection of 1863 bursts in a period from April 1 to June 11, 2021 (Xu et al. 2022). Four months later, another active episode was also observed by FAST with detection of over 600 bursts in a period of 4 days (Zhou et al. 2022; Zhang et al. 2022; Jiang et al. 2022; Niu et al. 2022). Interestingly, comparison of the observed burst property distributions between the two burst episodes, including the spectral width, burst energy, and peak frequency, shows that they are statistically consistent. This may hint the bursts of the two episodes are from the same radiating region.

Acknowledgements. We thank the anonymous referee for helpful comments. We thank the helpful discussions with Yuan-Pei Yang, Yao Chen, Shu-Qing Zhong, Qi Wang and Ying Gu. We acknowledge the use of the public data from the FAST/FRB Key Project. This work is supported by National Key R&D Program (2024YFA1611700) and the National Natural Science Foundation of China (grant Nos. 12403042, 12133003, 12203013 and 12203022). E. W. L. is supported by the Guangxi Talent Program (“Highland of Innovation Talents”).

References

- Aggarwal, K., Agarwal, D., Lewis, E. F., et al. 2021, *ApJ*, 922, 115
- Aleksandrov, A. F., Bogdankevich, L. S., & Rukhadze, A. A. 1984, in *Berlin and New York*, Vol. 9, 2444
- Beloborodov, A. M. 2017, *ApJ*, 843, L26
- Beloborodov, A. M. 2020, *ApJ*, 896, 142
- Bhardwaj, M., Gaensler, B. M., Kaspi, V. M., et al. 2021, *ApJ*, 910, L18
- Bochenek, C. D., Ravi, V., Belov, K. V., et al. 2020, *Nature*, 587, 59
- Caleb, M., Stappers, B. W., Rajwade, K., & Flynn, C. 2019, *MNRAS*, 484, 5500
- Chatterjee, S., Law, C. J., Wharton, R. S., et al. 2017, *Nature*, 541, 58
- CHIME/FRB Collaboration, Amiri, M., Andersen, B. C., et al. 2021, *ApJS*, 257, 59
- Chime/Frb Collaboration, Andersen, B. C., Bandura, K., et al. 2023, *ApJ*, 947, 83
- CHIME/FRB Collaboration, Andersen, B. C., Bandura, K. M., et al. 2020, *Nature*, 587, 54
- Cordes, J. M. & Chatterjee, S. 2019, *ARA&A*, 57, 417
- Cruces, M., Spitler, L. G., Scholz, P., et al. 2021, *MNRAS*, 500, 448
- Dai, Z. G., Wang, J. S., Wu, X. F., & Huang, Y. F. 2016, *ApJ*, 829, 27
- Deng, C.-M. 2021, *Phys. Rev. D*, 103, 123030
- Deng, C.-M., Zhong, S.-Q., & Dai, Z.-G. 2021, *ApJ*, 922, 98
- Feng, Y., Li, D., Yang, Y.-P., et al. 2022, *Science*, 375, 1266
- Fonseca, E., Andersen, B. C., Bhardwaj, M., et al. 2020, *ApJ*, 891, L6
- Gajjar, V., Siemion, A. P. V., Price, D. C., et al. 2018, *ApJ*, 863, 2
- Geng, J., Li, B., & Huang, Y. 2021, *The Innovation*, 2, 100152
- Ghisellini, G. 2017, *MNRAS*, 465, L30
- Ginzburg, V. L. 1989, *Applications of electrodynamics in theoretical physics and astrophysics*.
- Gourdji, K., Michilli, D., Spitler, L. G., et al. 2019, *ApJ*, 877, L19
- Gruzinov, A. & Waxman, E. 2019, *ApJ*, 875, 126
- Hankins, T. H. & Eilek, J. A. 2007, *ApJ*, 670, 693
- Hankins, T. H., Eilek, J. A., & Jones, G. 2016, *ApJ*, 833, 47
- Hessels, J. W. T., Spitler, L. G., Seymour, A. D., et al. 2019, *ApJ*, 876, L23
- Hewitt, D. M., Snelders, M. P., Hessels, J. W. T., et al. 2022, *MNRAS*, 515, 3577
- Houben, L. J. M., Spitler, L. G., ter Veen, S., et al. 2019, *A&A*, 623, A42
- Jiang, J.-C., Wang, W.-Y., Xu, H., et al. 2022, *Research in Astronomy and Astrophysics*, 22, 124003
- Jiang, P., Yue, Y., Gan, H., et al. 2019, *Science China Physics, Mechanics, and Astronomy*, 62, 959502
- Joseph, A., Chawla, P., Fonseca, E., et al. 2019, *ApJ*, 882, L18
- Karlický, M. 2013, *A&A*, 552, A90
- Katz, J. I. 2020, *MNRAS*, 494, L64
- Keane, E. F., Stappers, B. W., Kramer, M., & Lyne, A. G. 2012, *MNRAS*, 425, L71
- Khangulyan, D., Barkov, M. V., & Popov, S. B. 2022, *ApJ*, 927, 2
- Kong, X., Guo, F., Chen, Y., & Giacalone, J. 2019, *ApJ*, 883, 49
- Kumar, P., Lu, W., & Bhattacharya, M. 2017, *MNRAS*, 468, 2726
- Kumar, P., Shannon, R. M., Flynn, C., et al. 2021, *MNRAS*, 500, 2525
- Law, C. J., Abruzzo, M. W., Bassa, C. G., et al. 2017, *ApJ*, 850, 76
- Li, D., Wang, P., Zhu, W. W., et al. 2021, *Nature*, 598, 267
- Liu, Z.-N., Geng, J.-J., Yang, Y.-P., Wang, W.-Y., & Dai, Z.-G. 2023, *ApJ*, 958, 35
- Long, K. & Pe'er, A. 2018, *ApJ*, 864, L12
- Lorimer, D. R., Bailes, M., McLaughlin, M. A., Narkevic, D. J., & Crawford, F. 2007, *Science*, 318, 777
- Lu, W., Kumar, P., & Zhang, B. 2020, *MNRAS*, 498, 1397
- Lyu, F., Cheng, J.-G., Liang, E.-W., et al. 2022, *ApJ*, 941, 127
- Lyu, F. & Liang, E.-W. 2023, *MNRAS*, 522, 5600
- Lyu, F., Liang, E.-W., & Li, D. 2024, *ApJ*, 966, 115
- Lyu, F., Meng, Y.-Z., Tang, Z.-F., et al. 2021, *Frontiers of Physics*, 16, 24503
- Lyubarsky, Y. 2014, *MNRAS*, 442, L9
- Lyubarsky, Y. 2021, *Universe*, 7, 56
- Lyutikov, M., Burzawa, L., & Popov, S. B. 2016, *MNRAS*, 462, 941
- Macquart, J. P., Shannon, R. M., Bannister, K. W., et al. 2019, *ApJ*, 872, L19
- McCray, R. 1966, *Science*, 154, 1320
- Metzger, B. D., Margalit, B., & Sironi, L. 2019, *MNRAS*, 485, 4091
- Michilli, D., Seymour, A., Hessels, J. W. T., et al. 2018, *Nature*, 553, 182
- Niu, J.-R., Zhu, W.-W., Zhang, B., et al. 2022, *Research in Astronomy and Astrophysics*, 22, 124004
- Oostrum, L. C., Maan, Y., van Leeuwen, J., et al. 2020, *A&A*, 635, A61
- Pearlman, A. B., Majid, W. A., Prince, T. A., et al. 2020, *ApJ*, 905, L27
- Petroff, E., Barr, E. D., Jameson, A., et al. 2016, *PASA*, 33, e045
- Petroff, E., Hessels, J. W. T., & Lorimer, D. R. 2019, *A&A Rev.*, 27, 4
- Petroff, E., Hessels, J. W. T., & Lorimer, D. R. 2022, *A&A Rev.*, 30, 2
- Planck Collaboration, Ade, P. A. R., Aghanim, N., et al. 2016, *A&A*, 594, A13
- Platts, E., Weltman, A., Walters, A., et al. 2019, *Phys. Rep.*, 821, 1
- Pljunis, Z., Good, D. C., Kaspi, V. M., et al. 2021, *ApJ*, 923, 1
- Rajwade, K. M., Mickaliger, M. B., Stappers, B. W., et al. 2020, *MNRAS*, 495, 3551
- Rybicki, G. B. & Lightman, A. P. 1986, *Radiative Processes in Astrophysics*
- Sagiv, A. & Waxman, E. 2002, *ApJ*, 574, 861
- Sazonov, V. N. 1970, *Soviet Ast.*, 13, 797
- Scholz, P., Spitler, L. G., Hessels, J. W. T., et al. 2016, *ApJ*, 833, 177
- Spitler, L. G., Cordes, J. M., Hessels, J. W. T., et al. 2014, *ApJ*, 790, 101
- Spitler, L. G., Scholz, P., Hessels, J. W. T., et al. 2016, *Nature*, 531, 202
- Tendulkar, S. P., Bassa, C. G., Cordes, J. M., et al. 2017, *ApJ*, 834, L7
- Thornton, D., Stappers, B., Bailes, M., et al. 2013, *Science*, 341, 53
- Twiss, R. Q. 1958, *Australian Journal of Physics*, 11, 564
- Wang, J.-S., Yang, Y.-P., Wu, X.-F., Dai, Z.-G., & Wang, F.-Y. 2016, *ApJ*, 822, L7
- Wang, W.-Y., Yang, Y.-P., Li, H.-B., Liu, J., & Xu, R. 2024, *A&A*, 685, A87
- Waxman, E. 2017, *ApJ*, 842, 34
- Wild, J. P., Smerd, S. F., & Weiss, A. A. 1963, *ARA&A*, 1, 291
- Xiao, D., Wang, F., & Dai, Z. 2021, *Science China Physics, Mechanics, and Astronomy*, 64, 249501
- Xu, H., Niu, J. R., Chen, P., et al. 2022, *Nature*, 609, 685
- Yang, Y.-P. 2023, *ApJ*, 956, 67
- Yang, Y.-P., Lu, W., Feng, Y., Zhang, B., & Li, D. 2022, *ApJ*, 928, L16
- Yang, Y.-P. & Zhang, B. 2018, *ApJ*, 868, 31
- Zhang, B. 2018, *The Physics of Gamma-Ray Bursts*
- Zhang, B. 2020, *Nature*, 587, 45
- Zhang, B. 2022, *ApJ*, 925, 53
- Zhang, B. 2023, *Reviews of Modern Physics*, 95, 035005
- Zhang, Y., Geng, J.-J., & Huang, Y.-F. 2018a, *ApJ*, 858, 88
- Zhang, Y. G., Gajjar, V., Foster, G., et al. 2018b, *ApJ*, 866, 149
- Zhang, Y.-K., Li, D., Zhang, B., et al. 2023, *ApJ*, 955, 142
- Zhang, Y.-K., Wang, P., Feng, Y., et al. 2022, *Research in Astronomy and Astrophysics*, 22, 124002
- Zheleznyakov, V. V. 1967, *Soviet Journal of Experimental and Theoretical Physics*, 24, 381
- Zhong, S.-Q., Xie, W.-J., Deng, C.-M., et al. 2022, *ApJ*, 926, 206
- Zhou, D. J., Han, J. L., Zhang, B., et al. 2022, *Research in Astronomy and Astrophysics*, 22, 124001

Appendix A: Synchrotron self-absorption and the possibility of negative reabsorption

The synchrotron self-absorption coefficient obtained by the Einstein coefficient method is (Twiss 1958; Wild et al. 1963):

$$\alpha_v^{[p]} = -\frac{1}{4\pi m_e v^2} \int d\gamma_e \gamma_e^2 P_v^{[p]}(\gamma_e) \frac{d}{d\gamma_e} \left(\gamma_e^{-2} \frac{dn_e}{d\gamma_e} \right). \quad (\text{A.1})$$

Another expression is obtained according to integration by parts (Zheleznyakov 1967)

$$\alpha_v^{[p]} = \frac{1}{4\pi m_e v^2} \int d\gamma_e \gamma_e^{-2} \frac{dn_e}{d\gamma_e} \frac{d}{d\gamma_e} \left(\gamma_e^2 P_v^{[p]}(\gamma_e) \right) \quad (\text{A.2})$$

and the specific emissivity is defined as

$$j_v^{[p]} = \int \frac{P_v^{[p]}(\gamma_e) dn_e}{4\pi} \frac{d\gamma_e}{d\gamma_e}, \quad (\text{A.3})$$

where ν is the frequency, γ_e is the Lorentz factor of the electron, $P_v^{[p]}(\gamma_e)$ is the radiation power per unit frequency emitted by a single electron with Lorentz factor γ_e in a polarization $[p]$, and $\frac{dn_e}{d\gamma_e}$ is the isotropic distribution function of electrons. When the effect of plasma is considered,

$$P_v^{[p]}(\gamma_e) = \frac{2\pi e^2 v_c}{\sqrt{3}\gamma_e^2 c} S_v^{-1/2}(\gamma_e) \left[x f^{[p]}(x) \right]_{x=S_v^{3/2} v/\gamma_e} \quad (\text{A.4})$$

with

$$f^{\{\perp, \parallel\}}(x) = \pm K_{2/3}(x) + \int_x^\infty dy K_{5/3}(y),$$

$$v_c = \gamma_e^3 v_B \sin \chi = \gamma_e^2 \frac{3eB \sin \chi}{4\pi m_e c}, \quad S_v(\gamma_e) = 1 + \left(\frac{\gamma_e v_P}{v} \right)^2$$

and χ is the electron pitch angle, $K_{5/3}$ and $K_{2/3}$ is the modified Bessel function. In the case of electron distribution as a delta function, $\frac{dn_e}{d\gamma_e} = \delta(\gamma_e - \gamma_{e,s})$, the self-absorption coefficient can be estimated as (Waxman 2017)

$$\alpha_v^{[p]}(g, y) = 2\alpha_0 y^{-3} \left[f^{[p]}(x) + \left(\frac{1}{2} - \frac{y^2}{g} \right) x \frac{df(x)^{[p]}}{dx} \right] \quad (\text{A.5})$$

with

$$x = y(g^{-1} + y^{-2})^{3/2} / \sin \chi, \quad \alpha_0 = \frac{\pi v_B}{2\sqrt{3}c} \sqrt{\frac{v_B}{v_P}} \sin \chi$$

and the specific emissivity can be estimated as

$$j_v^{[p]}(g, y) = j_0 \left(1 + \frac{g}{y^2} \right)^{-1/2} g \left[x f^{[p]}(x) \right] \quad (\text{A.6})$$

with

$$x = y(g^{-1} + y^{-2})^{3/2} / \sin \chi, \quad j_0 = \frac{\pi m_e}{2\sqrt{3}c} v_P^3 \sin \chi.$$

When the effect of plasma is ignored, as in the case of a vacuum,

$$P_v^{[p]'}(\gamma_e) = \frac{2\pi e^2 v_c'}{\sqrt{3}\gamma_e^2 c} \left[x' f^{[p]}(x') \right]_{x'=v/\gamma_e'} \quad (\text{A.7})$$

with

$$f^{[p]}(x') = \pm K_{2/3}(x') + \int_{x'}^\infty dy K_{5/3}(y),$$

$$v_c' = \gamma_e^3 v_B \sin \chi = \gamma_e^2 \frac{3eB \sin \chi}{4\pi m_e c}$$

and χ is the electron pitch angle, $K_{5/3}$ and $K_{2/3}$ is the modified Bessel function. The self-absorption coefficient produced by the electron distribution as a delta function can be estimated as

$$\alpha_v^{[p]'}(g, y) = 2\alpha_0' y^{-3} \left[-\frac{y^2}{g} x' \frac{df(x')^{[p]}}{dx'} \right] \quad (\text{A.8})$$

with

$$x' = y/(g^{3/2} \sin \chi), \quad \alpha_0' = \frac{\pi v_B}{2\sqrt{3}c} \sqrt{\frac{v_B}{v_P}} \sin \chi,$$

where $g = \gamma_{e,s}^2 \frac{v_B}{v_P}$, $y = \frac{v}{v_R^*}$, $v_R^* = \sqrt{\frac{v_P}{v_B}} v_P$, v_B is the cyclotron frequency of relativistic electrons, v_P is the relativistic plasma frequency.